Supplementary Information (SI) for Journal of Materials Chemistry B.

Supporting Information

Multifunctional carbon dots-based dual-channel and dual-signal sensors for ribonucleotide discrimination and Fe^{3+} detection

Runjie Miao [a,b], *Yu Zhang* [a,b], *Haifeng Sha* [a]*, *Wenyan Ma* [a,c], *Yuefeng Huang* [a,c], *Hangrong Chen* [a,c]*

a, State Key Laboratory of High Performance Ceramics and Superfine Microstructure, Shanghai Institute of Ceramics, Chinese Academy of Sciences, 1295 Ding-Xi Road, Shanghai 200050, China.

b, Center of Materials Science and Optoelectronics Engineering, University of Chinese Academy of Sciences, 19A Yuquan Road, Beijing 100049, China

c, School of Chemistry and Materials Science, Hangzhou Institute for Advanced Study, University of Chinese Academy of Sciences, 1 Sub-lane Xiangshan, Hangzhou 310024, China

*Correspondence author. E-mail addresses: hrchen@mail.sic.ac.cn (H. Chen), shahaifeng@mail.sic.ac.cn (H. Sha)

1. Chemicals and Characterizations

1.1 Chemicals: Resorcinol, $CuSO_4 \cdot 5H_2O$, tetraethyl orthosilicate (TEOS), octadecyltrimethoxysilane (ODMS, 85%), dimethyl sulfoxide (DMSO), bovine serum albumin (BSA), β-D-Glucose (Glu), needle filter (mixed cellulose, 0.22 μm), and dialysis membrane (MWCO of 200 Da) were purchased from Aladdin. Sodium L-Ascorbyl-2-Phosphate (AAP), $FeCl_3$, $MgCl_2$, $ZnSO_4 \cdot 7H_2O$, K_2SO_4, L-Tryptophan (L-Trp), L-Ascorbic Acid (L-AA), adenosine triphosphate (ATP), adenosine diphosphate (ADP), adenosine monophosphate (AMP), guanosine triphosphate (GTP), guanosine diphosphate (GDP), guanosine monophosphate (GMP), uridine triphosphate (UTP), uridine diphosphate (UDP), uridine monophosphate (UMP), cytidine triphosphate (CTP), cytidine diphosphate (CDP), and cytidine monophosphate (CMP) were purchased from Rhawn. AIE molecules (MeTTPy) were supplied by Xarxbio (Xi' an, China). Urea (UR), $FeSO_4 \cdot 7H_2O$, $MnSO_4 \cdot H_2O$, NaCl, $CaCl_2 \cdot H_2O$, $NaHCO_3$, ammonia (25-28%), and ethanol were purchased from Sinopharm. Fetal bovine serum was purchased from Gibco Company in the United States. All the chemical agents used were of analytic grade.

1.2 Characterizations: Transmission electron microscopic (TEM) images were obtained by a JEM-2100F transmission electron microscope operated at 200 kV. Hydrodynamic diameters and zeta potentials were measured by a Zetasizer Nanoseries (Nano ZS90). The fluorescence spectra were recorded by a Shimadzu RF-6000 fluorospectrophotometer. The UV-vis spectra were performed on a Shimadzu UV-3600 spectrophotometer. The Brunauer-Emmett-Teller (BET) surface area was measured by a Specific Surface Area Analyzer (Micromeritics Tristar 3000). The powder X-ray diffraction (XRD) patterns were obtained on a Rigaku D/Max-2550 V diffractometer with a Cu Kα radiation source (40 kV, 40 mA). The water contact angles were measured by a drop-shaped analysis system (Solon Tech SL200B). X-ray photoelectron spectroscopy (XPS) analysis was conducted on a Thermo ESCAlab250. Fourier transform infrared (FT-IR) spectra were performed on a Bruker Vertex 70 FTIR spectrometer. The fluorescence quantum yield was measured using the Edinburgh SFL1000. Fluorescence lifetime decay curves were measured by using the steady-state transient fluorescence spectrometer F-4600. All fluorescent photos were taken with a smartphone under a UV lamp (365 nm).

2. Experimental Section

2.1 Synthesis of hMSNA

Firstly, a mixture of C_{18}TMS (ODMS) (2 mL) and TEOS (5 mL) was added to a mixture of ethanol (142.8 mL), deionized water (20 mL), and ammonia (3.14 mL). The mixture was stirred at 30 °C for 60 min. The materials were washed and freeze-dried to obtain hydrophobic porous silica nanoparticles (**hMSN)**. Then, disperse hMSN (20 mg) in DMSO (1.7 mL) and add the DMSO solution of AIE molecules (150 μL, 1 mg mL^{-1}), which was stirred at room temperature for 4 h, washed with ethanol, and dispersed in 2 mL of deionized water for later use. The product was named **hMSNA**.

2.2 Fluorescence detection for Fe^{3+}

2.2.1 The detection of Fe^{3+} by the dual-signal sensing system. According to the optimal conditions, a mixed solution of Cu-CDs, hMSNA, and AAP was prepared and diluted to 1.6 mL with deionized water to ensure that the final concentrations of the above components in the mixed system were 0.020 mg mL^{-1}, 0.525 mg mL^{-1}, and 1.25 mM, respectively. Different concentrations of Fe^{3+} were added (400 μL), incubated for 2 min, and fluorescence spectra (Ex=371 nm) and fluorescence photos were recorded.

2.2.2 The detection of Fe^{3+} by the single-signal probe. The mixed solution of Cu-CDs and AAP was prepared and diluted to 1.6 mL with deionized water to ensure that the final concentrations of the above components in the mixed system were 0.020 mg mL^{-1} and 1.25 mM, respectively. Different concentrations of Fe^{3+} were added (400 μL), incubated for 2 min, and fluorescence spectra (Ex=371 nm) and fluorescence photographs were recorded.

2.2.3 The detection of Fe^{3+} by the single-signal probe. The mixed solution of hMSNA and AAP was prepared and diluted to 1.6 mL with deionized water to ensure that the final concentrations of the above components in the mixed system were 0.525 mg mL^{-1} and 1.25 mM, respectively. Different concentrations of Fe^{3+} were added (400 μL), incubated for 2 min, and fluorescence spectra (Ex=371 nm) and fluorescence photographs were recorded.

2.2.4 Detection of Fe^{3+} in real samples. Fetal bovine serum was first mixed with acetonitrile in a volume ratio of 1:1, allowed to stand for 5 min, centrifuged, the supernatant removed, and diluted 10 times with deionized water to obtain diluted serum. Diluted serum was used as a solvent to prepare Fe^{3+} solutions of different concentrations, which were used as the actual required serum samples. Then, the Fe^{3+} detection steps were repeated using the ratiometric fluorescence sensing system to investigate the performance of the ratio fluorescence sensing system in real samples.

2.3 Anti-interferenc performance of the dual-signal sensing system

Cu^{2+}, Zn^{2+}, Mn^{2+}, Fe^{2+}, Mg^{2+}, K^{+}, Na^{+}, Ca^{2+}, HCO_3^{-}, tryptophan (L-Trp), bovine serum albumin (BSA), and β-D-glucose (Glu) were used to assess the anti-interferenc performance of the dual-signal sensing system for Fe^{3+} detection.

3. Additional Data

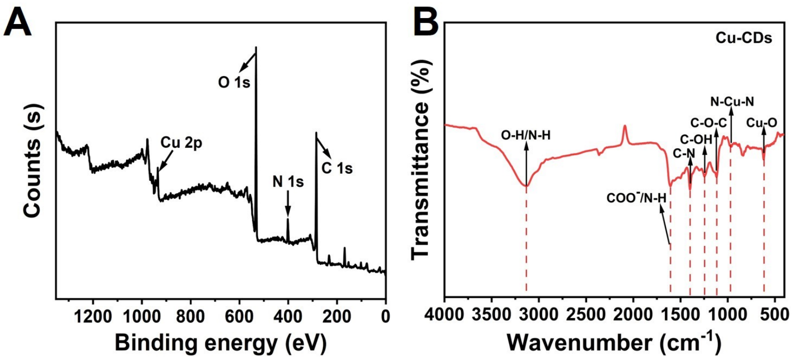

Figure S1. (A) XPS full spectrum of Cu-CDs. (B) FT-IR spectrum of Cu-CDs.

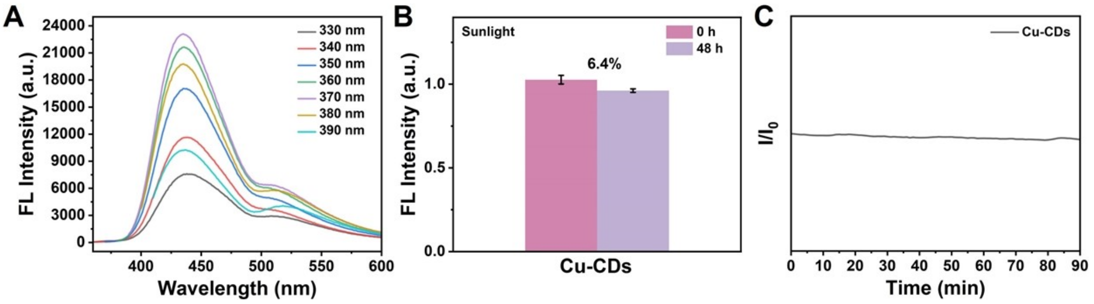

Figure S2. (A) FL emission spectra of the Cu-CDs at the different excitation wavelengths. (B) FL stability of Cu-CDs stored in sunlight for 48 h. (C) The photostability of Cu-CDs under excitation at 371 nm.

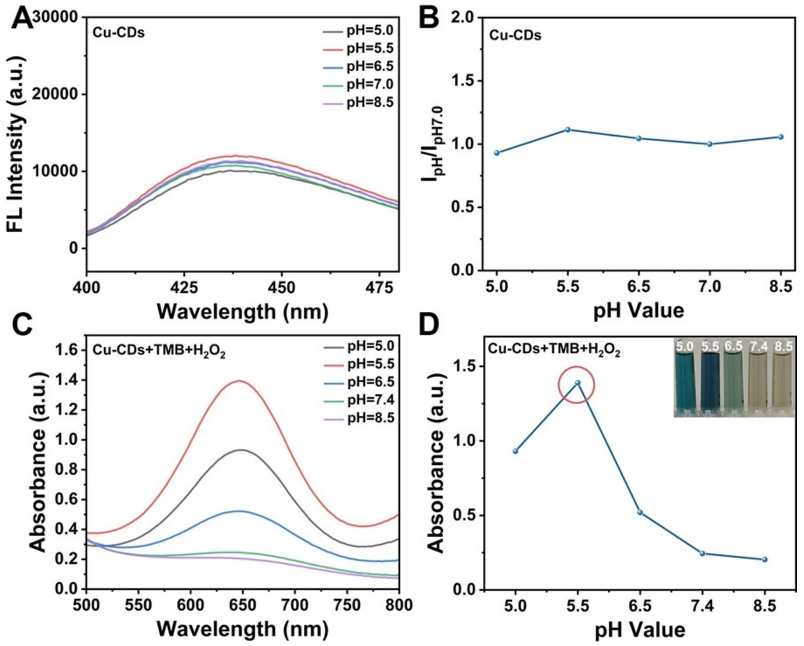

Figure S3. (A) FL emission spectra of the Cu-CDs at the different pH values. (Ex=371 nm). (B) The FL intensity ratio ($I_{pH}/I_{pH7.0}$) of Cu-CDs (Em=435 nm) to various pH values. (C) UV-vis absorption spectra of Cu-CDs+TMB+H_2O_2 at the different pH values. (D) UV-vis absorbance of Cu-CDs+TMB+H_2O_2 at 650 nm to various pH values. Inset: the corresponding photos under daylight.

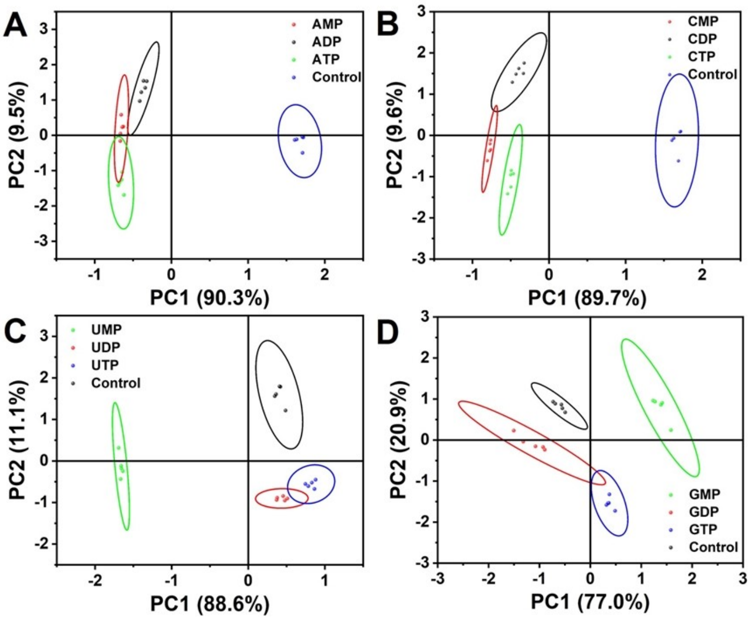

Figure S4. PCA diagrams of Cu-CDs response to different ribonucleotides (100 μM). (A) AMP, ADP, and ATP. (B) CMP, CDP, and CTP. (C) UMP, UDP, and UTP. (D) GMP, GDP, and GTP.

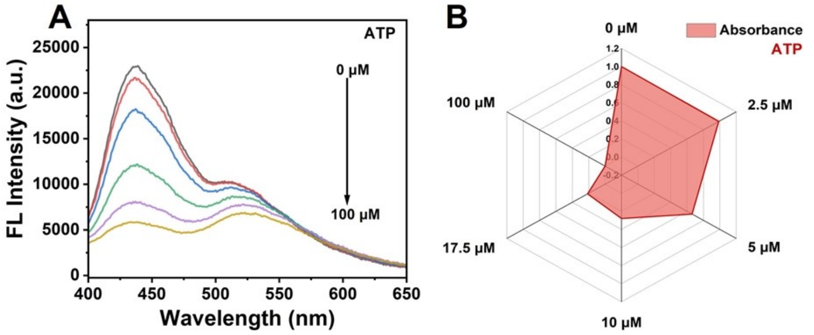

Figure S5. FL spectra (Ex=371 nm) (A) and normalized UV-vis absorbance at 650 nm (B) of Cu-CDs responding to different concentrations of ATP.

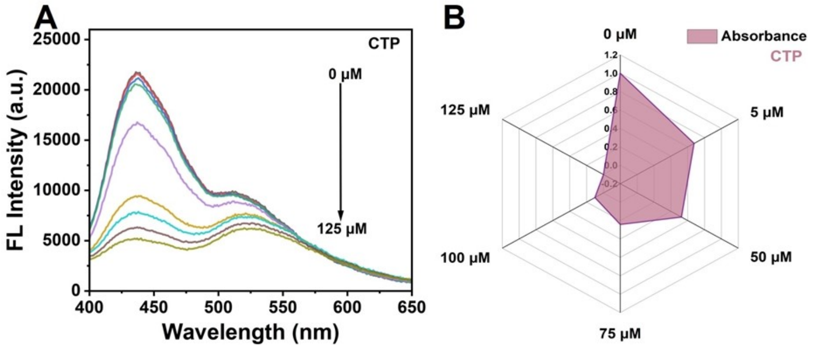

Figure S6. FL spectra (Ex=371 nm) (A) and normalized UV-vis absorbance at 650 nm (B) of Cu-CDs responding to different concentrations of CTP.

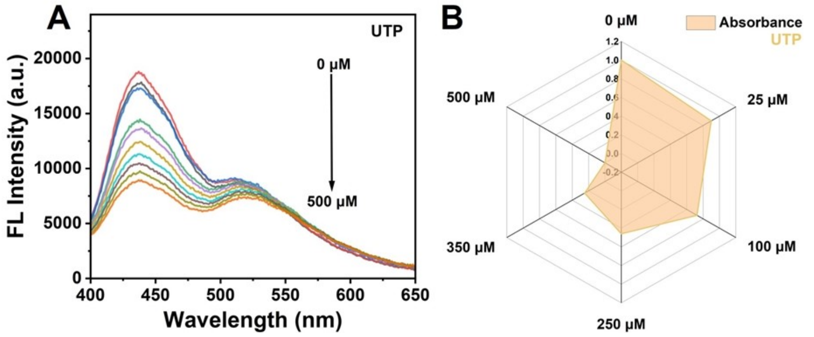

Figure S7. FL spectra (Ex=371 nm) (A) and normalized UV-vis absorbance at 650 nm (B) of Cu-CDs responding to different concentrations of UTP.

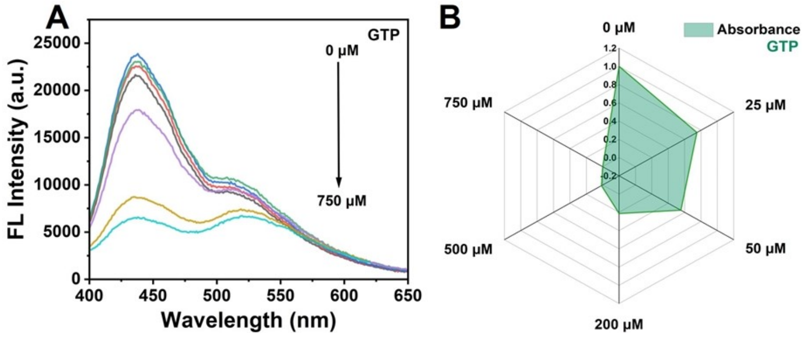

Figure S8. FL spectra (Ex=371 nm) (A) and UV-vis absorbance at 650 nm (B) of Cu-CDs responding to different concentrations of GTP.

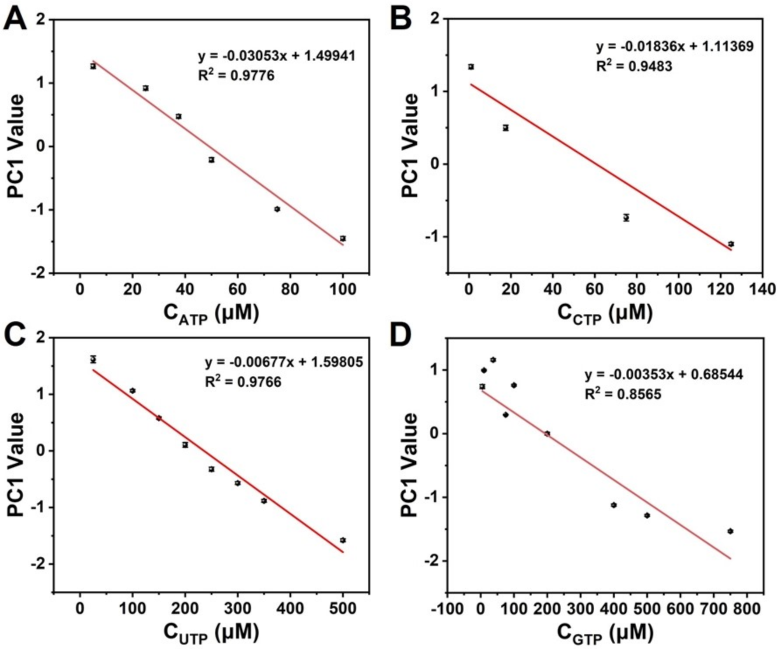

Figure S9. Linear relationships of ATP (A), CTP (B), UTP (C), and GTP (D) versus PC1 values.

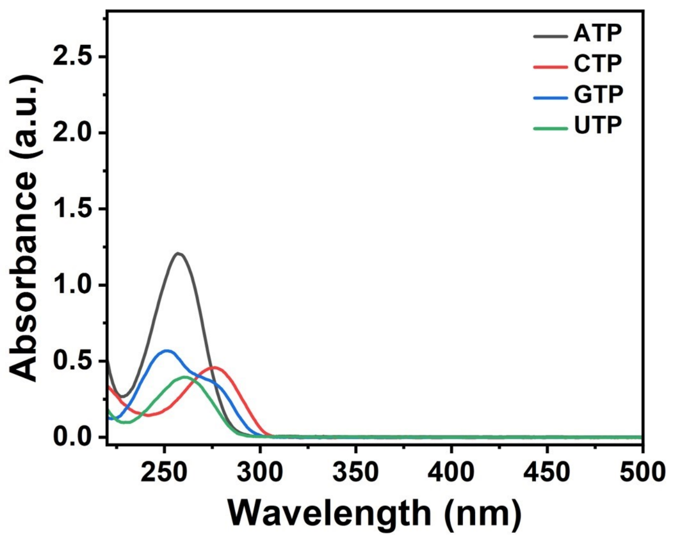

Figure S10. UV-vis absorption spectra of ATP, CTP, UTP, and GTP.

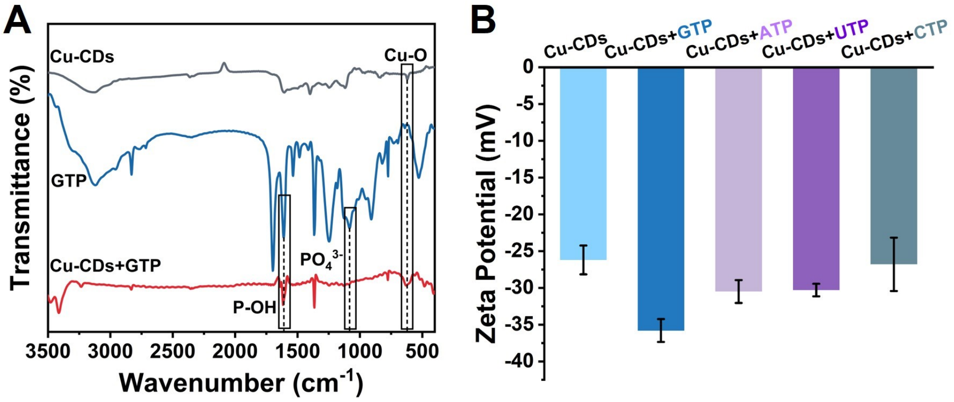

Figure S11. (A) FT-IR spectrum of Cu-CDs, GTP, and Cu-CDs+GTP. (B) Zeta Potential of Cu-CDs, Cu-CDs+GTP, Cu-CDs+ATP, Cu-CDs+UTP, and Cu-CDs+CTP.

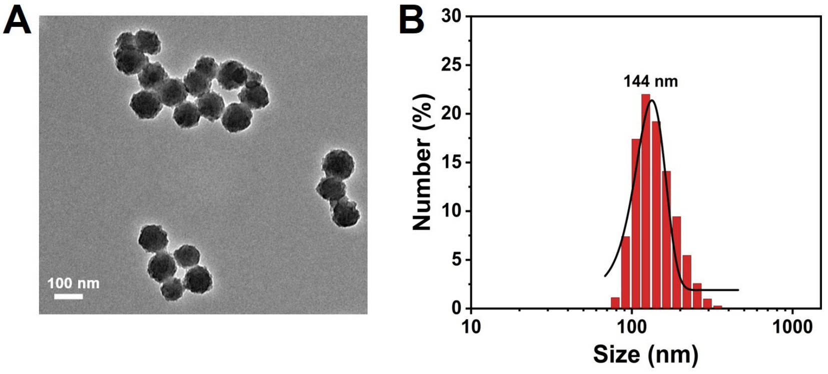

Figure S12. (A) TEM image of hMSNA. (B) Size distribution of hMSNA

(PDI=0.132).

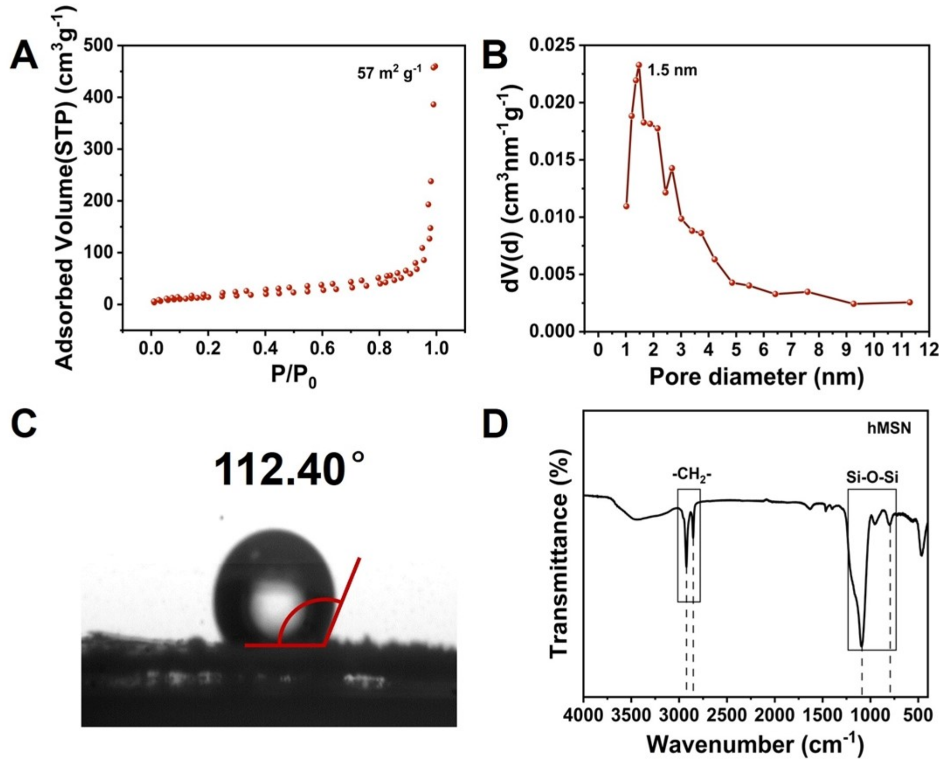

Figure S13. (A) N_2 adsorption-desorption isotherm. (B) Pore size distribution and (C) Water contact angle of hMSN. (D) FT-IR spectrum of hMSN.

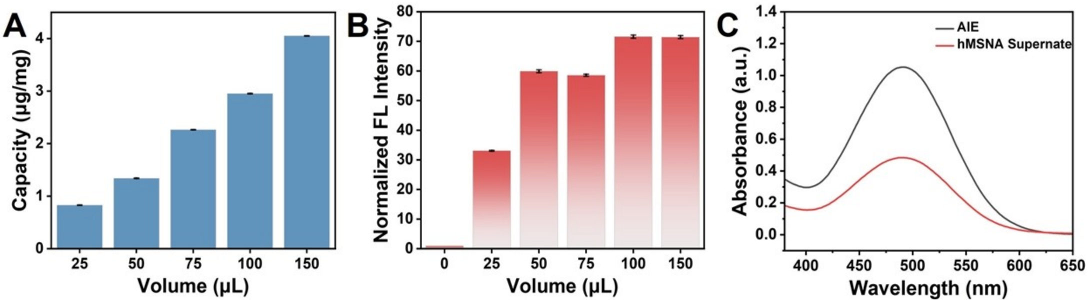

Figure S14. (A) The loading capacity and (B) Normalized FL intensity of hMSN on different volumes of AIE molecules. (C) UV-vis absorption spectra of AIE molecules and the supernate of hMSNA.

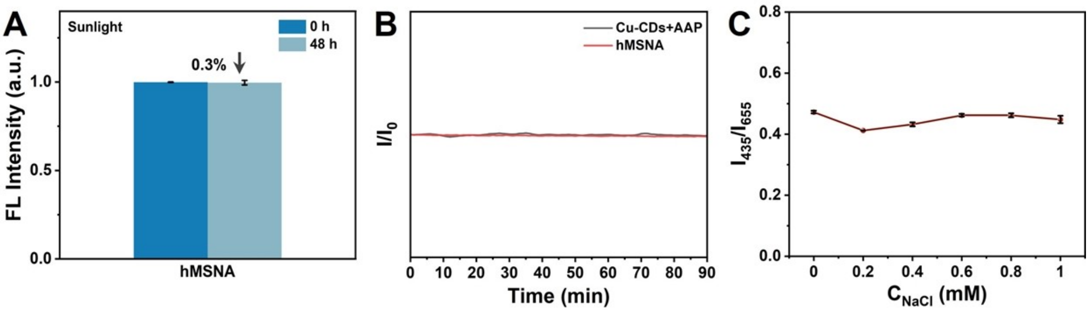

Figure S15. (A) FL stability of hMSNA stored in sunlight for 48 h. (B) The photostability of hMSNA and Cu-CDs+AAP under excitation at 545 nm and 371 nm, respectively. (C) The FL intensity ratio (I_{435}/I_{655}) of Cu-CDs and hMSNA to various concentration of NaCl aqueous solution.

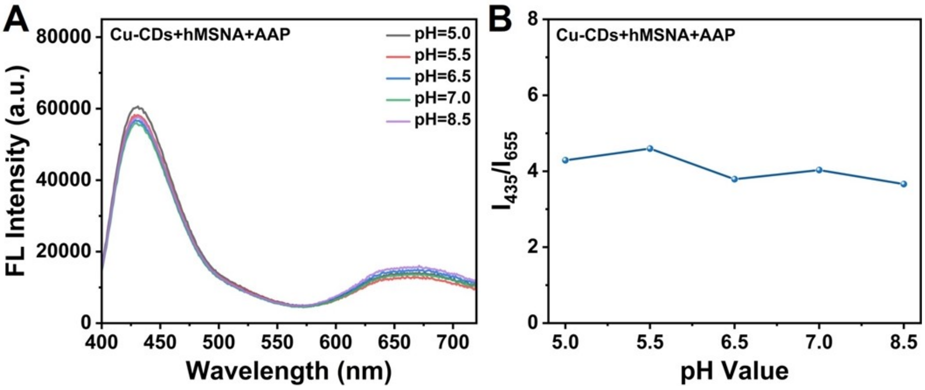

Figure S16. (A) FL spectra of the Cu-CDs+hMSNA+AAP at the different pH values. (Ex=371 nm). (B) The FL intensity ratio (I_{435}/I_{655}) of Cu-CDs+hMSNA+AAP to various pH values.

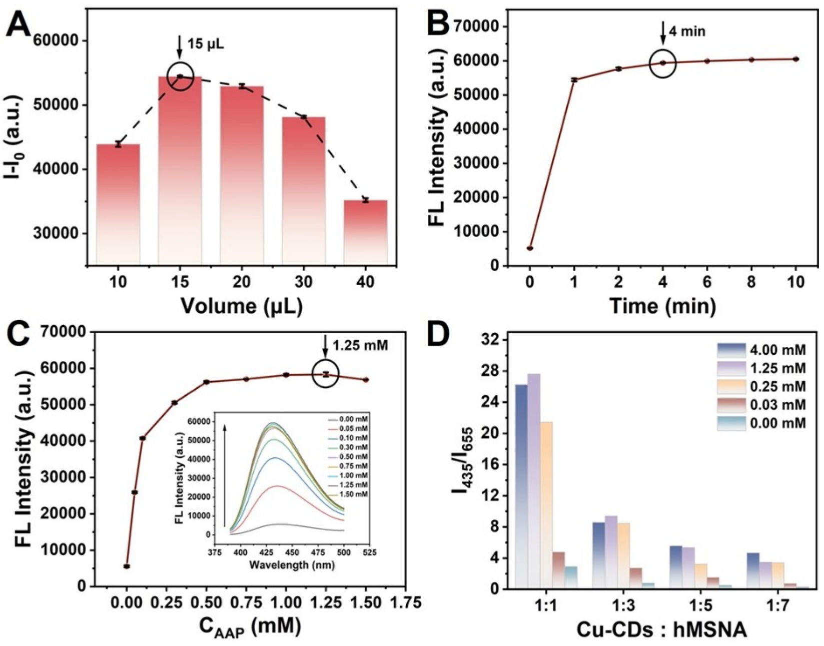

Figure S17. (A) The FL intensity changes of Cu-CDs with different volumes in response to AAP. Effect of reaction time (B) and different concentrations of AAP (C) on FL intensity of Cu-CDs (Ex=371 nm, Em=435 nm). (D) FL intensity ratio (I_{435}/I_{655}) of the Cu-CDs to hMSNA under different volume ratio (1:1, 1:3, 1:5, and 1:7) and different AAP concentrations (0, 0.03, 0.25, 1.25, and 4.00 mM).

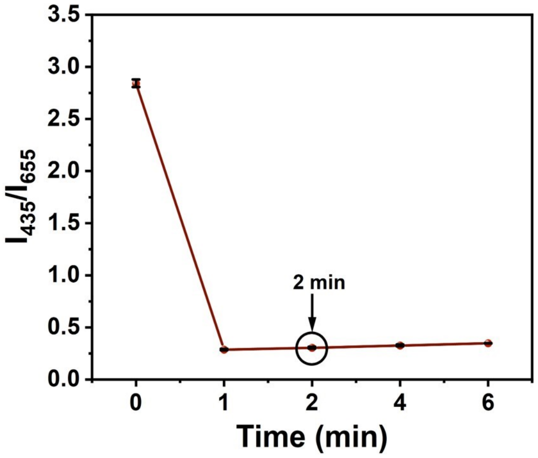

Figure S18. Changes of FL intensity ratio (I_{435}/I_{655}) of Cu-CDs to hMSNA with reaction time after addition of Fe^{3+} (1.25 mM).

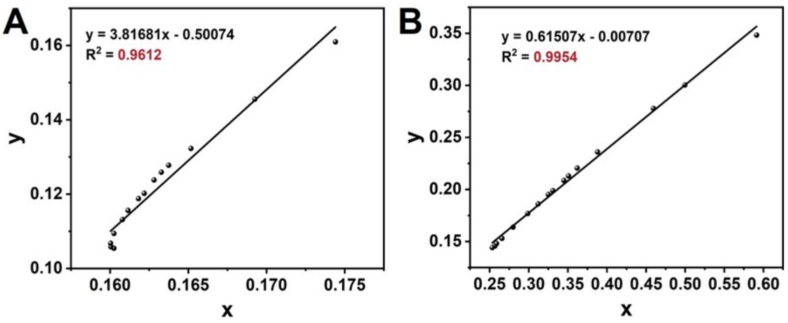

Figure S19. The linear fitting diagram of CIE of (A) Cu-CDs+AAP and (B) Cu-CDs+hMSNA+AAP to Fe^{3+} (0-400 μM).

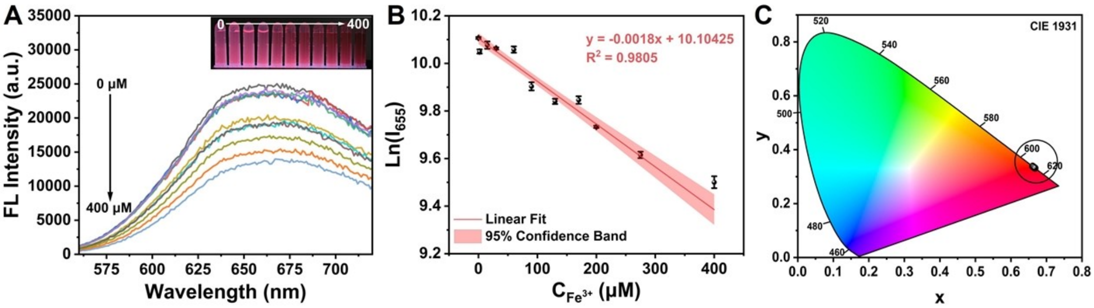

Figure S20. (A) FL spectra of hMSNA+AAP with increasing Fe^{3+} concentration (0-400 μM). The inset: the corresponding fluorescence images under UV light and (B) the relationship between $Ln(I_{655})$ and Fe^{3+} concentration diagram (Ex=371 nm). (C) CIE chromaticity diagram of hMSNA+AAP to Fe^{3+}.

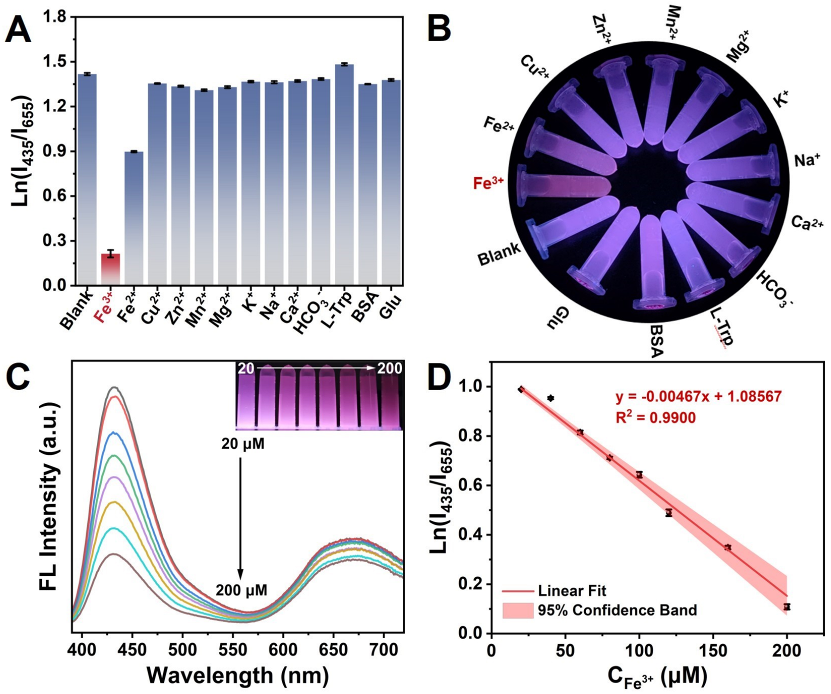

Figure S21. (A) Anti-interference test to Fe^{3+} of interfering substances (200 μM) (Fe^{2+}, Cu^{2+}, Zn^{2+}, Mn^{2+}, Mg^{2+}, K^{+}, Na^{+}, Ca^{2+}, HCO_3^{-}, L-Trp, BSA, and Glu). (B) Corresponding fluorescence images under UV light. (C) FL spectra of Cu-CDs+hMSNA+AAP with increasing Fe^{3+} concentration in serum (20-200 μM). The inset: the corresponding fluorescence images under UV light. (D) The diagram of the relationship between $Ln(I_{435}/I_{655})$ and Fe^{3+} concentration (Ex=371 nm).

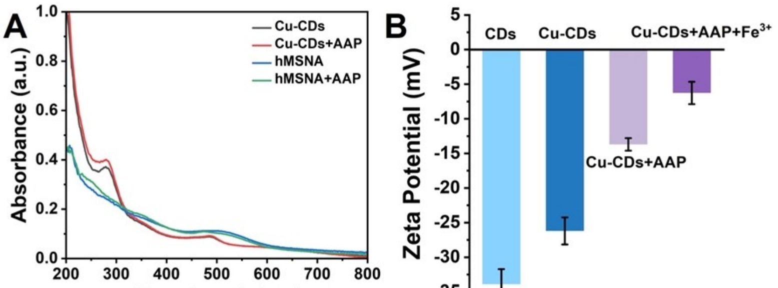

Figure S22. (A) UV-vis absorption spectra of Cu-CDs, Cu-CDs+AAP, hMSNA, and hMSNA+AAP. (B) Zeta Potential of CDs, Cu-CDs, Cu-CDs+AAP, and Cu-CDs+AAP+Fe^{3+}.

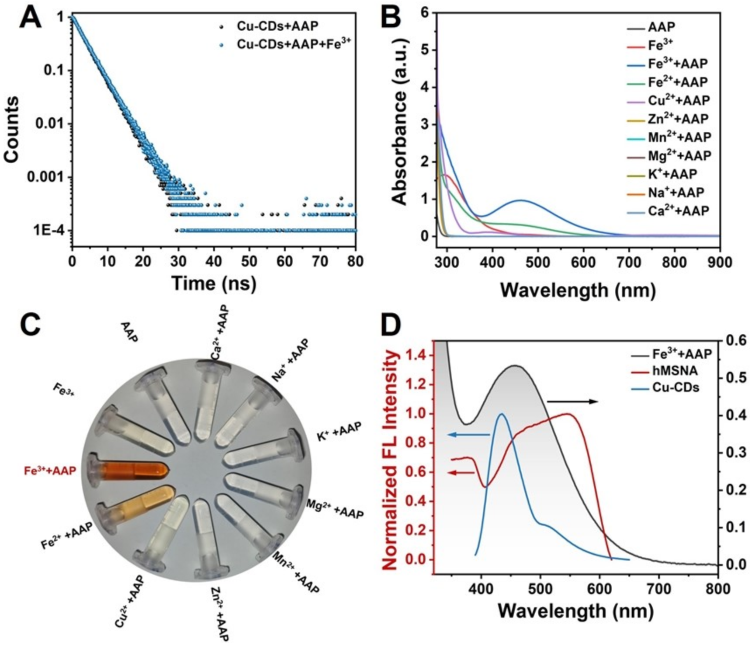

Figure S23. (A) Fluorescence lifetime scatter plots of Cu-CDs+AAP, Cu-CDs+AAP+Fe^{3+}. UV-vis absorption spectra of AAP, Fe^{3+}, and metal ions+AAP (B) and corresponding photos (C). (D) UV-vis absorption spectrum of Fe^{3+}+AAP, FL excitation spectrum of hMSNA, and FL emission spectrum of Cu-CDs.

Table S1. Fluorescence lifetime decay related parameters for Cu-CDs, Cu-CDs+ATP, Cu-CDs+UTP, Cu-CDs+CTP, and Cu-CDs+GTP.

Compounds	**λ_{ex}(nm)**	**λ_{em}(nm)**	**A_1**	**τ_1(ns)**	**A_2**	**τ_2(ns)**	**τ_{avg}(ns)**
Cu-CDs	375	435	0.601	0.449	0.966	3.610	3.383
Cu-CDs+ATP	375	435	2.504	0.375	0.440	3.657	2.447
Cu-CDs+UTP	375	435	2.700	0.337	0.251	3.655	2.003
Cu-CDs+CTP	375	435	2.455	0.458	0.244	3.786	1.959
Cu-CDs+GTP	375	435	1.061	0.430	0.639	3.530	3.008

$\tau_{avg}=(A_1\tau_1^2+A_2\tau_2^2)/(A_1\tau_1+A_2\tau_2)$, where τ_1 ,τ_2 represent the decay time constants of different radiative decay channels and A_1, A_2 are the corresponding amplitudes.

Table S2. Comparison of the established fluorescent assay with other fluorescent assays reporter in literatures for the detection of Fe^{3+}.

Signal mode	**Material**	**Linear Range (μM)**	**LOD (μM)**	**Time (min)**	**Visualization**	**Reference**
Single	AIE nanomicelles	10-90	1.04	5	No	[S1]
Single	Phenol-based organic probes	0-2.5	0.00017	8	Yes	[S2]
Single	near-infrared fluorescent probes	2-20	4.40	60	No	[S3]
Single	N, S doped carbon dots	0-50	0.11	-	No	[S4]
Single	La doped carbon dots	2.5-200	6.78	-	Yes	[S5]
Single	bis-triazole-based probe	0-1000	9.18	-	No	[S6]
Ratio	Terbium alginate encapsulated CsPbI3@Pb-MOF	0-90	0.44	8	No	[S7]
Ratio	Copper cluster	1-50	0.092	3	Yes	[S8]
Ratio	**Copper doped carbon dots&silica-based AIE materials**	**2-400**	**1.53**	**2**	**Yes**	**This work**

References

[S1] X. Hou, Y. Song, Y. Lv, P. Wang, K. Chen, G. Li and L. Guo, *Spectrochim. Acta, Part A*, 2023, **290**, 122254.

[S2] N. Duan, L. Ding, S. Yang, H. Tian and B. Sun, *Luminescence*, 2024, **39**, e70021.

[S3] Y. Shi, J. Yu, Y. Song, J. Fan, X. Wang, S. Li and H. Li, *Talanta*, 2025, **281**, 126944.

[S4] K. Annamalai, R. Ravichandran, A. Annamalai, A. Jeevarathinam, R. Suresh and S. Elumalai, *Mater. Res. Bull.*, 2025, **181**, 113068.

[S5] Q. Wang, Z. Wang, Z. Pu, Y. Wang and M. Li, *Opt. Mater.*, 2023, **137**, 113630.

[S6] S. Kumar, S. Gadiyaram, R. K. Tittal, G. Vikas D and R. Sharma, *J. Mol. Struct.*, 2023, **1290**, 135940.

[S7] Y. Hou, H. Feng, J. He, F. Meng, J. Sun, X. Li, X. Wang, Z. Su and C. Sun, *Dalton Transactions*, 2024, **53**, 2541-2550.

[S8] Y. Wang, J. Jian, B. Sun, Y. Wei, D. Pan, J. Cao and Y. Shen, *Sens. Actuators, B*, 2022, **370**, 132413.